

# Lagrangian tracer dynamics in a closed cylindrical turbulent convection cell

Mohammad S. Emran<sup>1</sup> and Jörg Schumacher<sup>\*1</sup>

<sup>1</sup>*Institut für Thermo- und Fluidodynamik, Technische Universität Ilmenau, Postfach 100565, D-98684 Ilmenau, Germany*

(Dated: October 11, 2018)

Turbulent Rayleigh-Bénard convection in a closed cylindrical cell is studied in the Lagrangian frame of reference with the help of three-dimensional direct numerical simulations. The aspect ratio of the cell  $\Gamma$  is varied between 1 and 12, and the Rayleigh number  $Ra$  between  $10^7$  and  $10^9$ . The Prandtl number  $Pr$  is fixed at 0.7. It is found that both the pair dispersion of the Lagrangian tracer particles and the statistics of the acceleration components measured along the particle trajectories depend on the aspect ratio for a fixed Rayleigh number for the parameter range covered in our studies. This suggests that large-scale circulations present in the convection cell affect the Lagrangian dynamics. Our findings are in qualitative agreement with existing Lagrangian laboratory experiments on turbulent convection.

PACS numbers: 47.55.pb, 47.27.te, 47.27.ek

## I. INTRODUCTION

The motion of a fluid can be described either in the Eulerian or Lagrangian frame of reference. In case of fluid turbulence, the Lagrangian point of view brought interesting and new insights on the small-scale structure and statistics (see e.g. Yeung [1], Toschi and Bodenschatz [2] for comprehensive reviews). These studies included intermittency of temporal velocity increments and accelerations [3–5] or the geometry of particle tracks [6]. Furthermore, two-particle and multi-particle dispersion have been analysed and compared with classical predictions by Batchelor [7] and Richardson [8].

Almost all of the experimental and numerical investigations in turbulent thermal convection have been conducted in the Eulerian frame. This includes studies on the turbulent heat transfer and large-scale circulations [9, 10] as well as on small-scale structures and dynamics of thermal plumes [11–13]. Recently, first Lagrangian laboratory experiments on convection were conducted in a closed cylindrical vessel [14] and numerical simulations were carried out in Cartesian slabs with periodic side walls and free-slip boundary conditions at the top and bottom [15, 16]. The focus of these studies was on the local variations of the heat transfer which can be measured along the trajectories of the Lagrangian tracers. In the numerical studies, these results could be connected to the local tracer accelerations. In the laterally infinitely extended layer (i.e. the configuration with periodic side walls), slightly less intermittent vertical accelerations  $a_z$  were detected in comparison to the lateral ones,  $a_x$  and  $a_y$ . This was manifested in the sparser tails of the probability density function (PDF) of  $a_z$ .

In the present work, we want to take these numerical Lagrangian studies to the next level. We report investigations in a closed cylindrical cell with no-slip boundary conditions at all walls. This is the characteristic setup

for almost all laboratory experiments. It will allow for a closer comparison with the work by Gasteuil *et al.* [14]. In addition, we want to explore systematically how the finite size of the cell affects the Lagrangian dynamics, such as the long-time behaviour of the two-particle dispersion. The latter point is also motivated by recent Eulerian studies, in which a systematic dependence of the turbulent heat transfer on the aspect ratio  $\Gamma$  is found for small and moderate values of  $\Gamma$  [17]. The dependence is in line with morphological changes in the large-scale circulation (LSC), e.g. from one-roll to multi-roll patterns, in the convection cell. Our boundary conditions will differ from those in Refs. [15, 16]. This difference might also affect the statistics of the acceleration components. It is thus another open question if a different velocity boundary layer structure has an impact on the intermittency of lateral and vertical acceleration components.

The outline of the paper is as follows. In section II we present the equations of motion, the numerical model and the tracer advection scheme for the non-uniform cylindrical mesh. Section III is focussed on the particle dynamics and local heat transfer followed by studies of the pair dispersion in Section IV and the aspect ratio dependence of the acceleration statistics in Section V. Finally, we summarize our findings and give a brief outlook.

## II. EQUATIONS OF MOTION AND NUMERICAL MODEL

### A. Boussinesq equations

We solve the Boussinesq equations for Rayleigh-Bénard convection numerically with a second-order finite difference scheme in cylindrical coordinates  $(\phi, r, z)$  [19, 20]. The equations are given by

$$\frac{\partial \mathbf{u}}{\partial t} + (\mathbf{u} \cdot \nabla) \mathbf{u} = -\nabla p + \nu \nabla^2 \mathbf{u} + \alpha g T e_z, \quad (1)$$

$$\nabla \cdot \mathbf{u} = 0, \quad (2)$$

<sup>\*</sup>Corresponding author: joerg.schumacher@tu-ilmenau.de

Run	$N_\phi \times N_r \times N_z$	$Ra$	$\Gamma$	$\pi\eta/\Delta$	$N_{BL}$
1	$193 \times 97 \times 128$	$10^7$	1	2.26	14
2	$257 \times 165 \times 128$	$10^7$	3	1.43	14
3	$361 \times 257 \times 128$	$10^7$	5	1.32	14
4	$401 \times 311 \times 128$	$10^7$	8	1.06	14
5	$601 \times 401 \times 128$	$10^7$	12	1.01	14
6	$271 \times 151 \times 256$	$10^8$	1	1.73	20
7	$361 \times 181 \times 310$	$10^9$	1	1.03	17

TABLE I: Simulation parameters for various  $Ra$  and  $\Gamma$  with a fixed  $Pr = 0.7$ . The grid resolution, the Rayleigh number  $Ra$ , the aspect ratio  $\Gamma$ , the ratio  $\pi\eta/\Delta$ , and  $N_{BL}$ , the number of horizontal grid planes inside the thermal boundary layer thickness, are given.  $N_{BL}$  satisfies the criteria discussed in [18] very well.

$$\frac{\partial T}{\partial t} + (\mathbf{u} \cdot \nabla)T = \kappa \nabla^2 T, \quad (3)$$

where  $p(\mathbf{x}, t)$  is the (kinematic) pressure,  $\mathbf{u}(\mathbf{x}, t)$  the velocity field,  $\alpha$  the thermal expansion coefficient and  $g$  the gravity acceleration. The velocity field has a no-slip boundary condition at all walls. The temperature field is isothermal at the top and bottom plates and adiabatic at the side wall. Following Refs. [13, 17], we have chosen the DNS grid such that the *global* maximum of the geometric mean of the grid spacings in  $\phi, r$  and  $z$ , i.e.

$$\Delta = \max_{\phi, r, z} [\sqrt[3]{r\Delta_\phi\Delta_r\Delta_z}], \quad (4)$$

satisfies the resolution threshold by Grötzbach [21], namely  $\pi\eta/\Delta > 1$  where  $\eta$  is the Kolmogorov dissipation length which is calculated via the mean energy dissipation rate  $\langle \epsilon \rangle = \frac{\nu^3}{H^4}(Nu - 1)RaPr^{-2}$ . The details are provided in Tab.1.

The resolutions of the runs are exactly the same as in [17]. Note that the turbulence is strongly inhomogeneous with respect to the vertical direction  $z$ . This results in amplitudes of the energy dissipation rate which are by orders of magnitude larger close to the plates than in the bulk. A local Kolmogorov scale is therefore much larger in the bulk as in the boundary layers. It motivated us in [17] to relate the grid spacing to  $\eta(z) = \nu^{3/4}/\langle \epsilon(z) \rangle_{A,t}$  rather than  $\eta$ .

The dimensionless parameters and their range of values in our numerical study are: the Rayleigh number  $Ra = \alpha g(T_{bottom} - T_{top})H^3/(\nu\kappa)$  between  $10^7$  and  $10^9$ , the Prandtl number  $Pr = \nu/\kappa = 0.7$  and the aspect ratios  $\Gamma = D/H$  between 1 and 12.  $D$  is the cell diameter and  $H$  is the height of the cell.

## B. Numerical integration scheme

We conduct direct numerical simulations (DNS) of the Boussinesq equations. The equations are solved in a

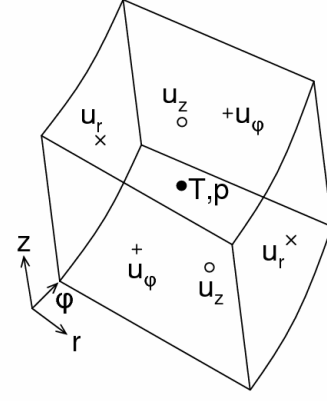


FIG. 1: Sketch of a 3D grid cell in the cylindrical coordinates, in which the positions of the velocity components, the temperature and the pressure are shown on the staggered grid.

cylindrical coordinate frame. The spatial discretization is performed on a staggered grid and solved by a second-order finite difference scheme [19, 20]. The pressure field  $p$  is determined by a two-dimensional Poisson solver [22] after applying one-dimensional fast Fourier transformations in the azimuthal direction. The time advancement is done by a third-order Runge-Kutta scheme. The grid spacings are non-equidistant in the radial and axial directions. In the vertical direction, they correspond to Tschebycheff collocation points. Some parameters and the corresponding grid resolutions are given in Table I.

## C. Tracer advection

The equations of Lagrangian tracer motion are given by

$$\frac{d\mathbf{x}_p(t)}{dt} = \mathbf{u}(\mathbf{x}_p, t). \quad (5)$$

Here  $\mathbf{u} = (u_\phi(\phi_p), u_r(r_p), u_z(z_p))^T$  is the velocity of the particle at position  $\mathbf{x}_p = (\phi_p(t), r_p(t), z_p(t))^T$  with the symbols  $\phi, r$  and  $z$  corresponding to the azimuthal, radial and axial directions, respectively. As discussed before, the Eulerian fields are well resolved on a staggered and non-uniform grid in the simulations. The velocity components, as shown in Fig. 1, are then given on particular faces of the grid cells only, while the Eulerian temperature field is always centered in the grid cell. All these fields are required at the Lagrangian particle position to advance (5) and study local heat transfer. We therefore applied an interpolation scheme for the velocity components which makes direct use of the staggered setup. The interpolation is then of second order and the maximal error can be estimated to be of the order of  $\mathcal{O}(\Delta^2)$  (see (4)). Given the Eulerian velocities at the mid points of the edges of the mesh cell (see Fig. 2), we

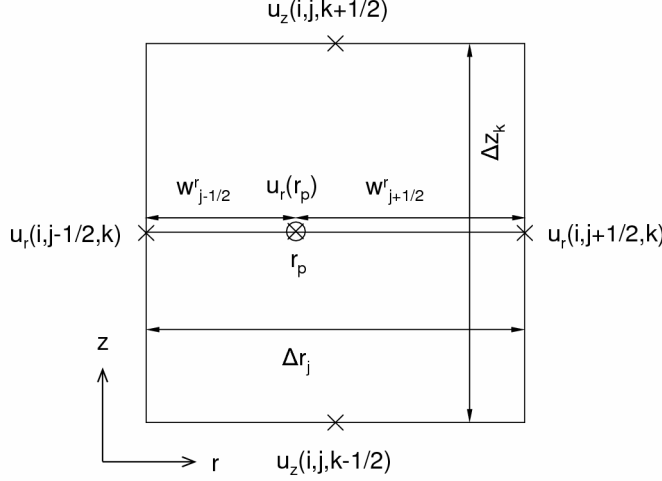


FIG. 2: Position of the velocity components on a 2D staggered grid in  $r-z$  plane, which is the mid section of a typical 3D cell as shown in the top panel of the figure. The indices  $i, j$  and  $k$  correspond to the azimuthal, radial and axial directions, respectively. The particle velocity  $u_r(r_p)$  at position  $r_p$  is obtained by the linear interpolation of the Eulerian velocities  $u_r(i, j - \frac{1}{2}, k)$  and  $u_r(i, j + \frac{1}{2}, k)$  with the widths  $w_{j-\frac{1}{2}}^r$  and  $w_{j+\frac{1}{2}}^r$  as given in (6).

calculate the corresponding Lagrangian components at an arbitrary position inside a cell as

$$\begin{aligned} u_r(r_p) &= \frac{w_{j-\frac{1}{2}}^r u_r(i, j + \frac{1}{2}, k) + w_{j+\frac{1}{2}}^r u_r(i, j - \frac{1}{2}, k)}{\Delta_r(i, j, k)}, \\ u_\phi(\phi_p) &= \frac{w_{i-\frac{1}{2}}^\phi u_\phi(i + \frac{1}{2}, j, k) + w_{i+\frac{1}{2}}^\phi u_\phi(i - \frac{1}{2}, j, k)}{\Delta_\phi(i, j, k)}, \\ u_z(z_p) &= \frac{w_{k-\frac{1}{2}}^z u_z(i, j, k + \frac{1}{2}) + w_{k+\frac{1}{2}}^z u_z(i, j, k - \frac{1}{2})}{\Delta_z(i, j, k)} \end{aligned} \quad (6)$$

Indices  $i, j, k$  denote the grid positions with respect to  $\phi, r, z$ , which run from 1 to  $N_\phi, N_r$  and  $N_z$ , respectively.

In order to progress further, we rewrite the three ordinary differential equations (we provide here details of the equation in  $r$ -direction only) [23] as

$$\frac{dr_p}{dt} = u_r(r_p) = \frac{r_p - r_L}{r_R - r_L} u_{r,R} + \left(1 - \frac{r_p - r_L}{r_R - r_L}\right) u_{r,L}, \quad (7)$$

where  $u_{r,R}$  and  $u_{r,L}$  are the Eulerian velocities at face positions  $r_R$  and  $r_L$ , respectively and  $r_p$  is the particle's position in between. The subscripts  $L$  and  $R$  refer to the left and right faces of a 3D-cell (see Fig. 1), respectively. Rearranging (7) yields [23]

$$\frac{dr_p}{dt} - r_p \frac{\Delta u_r}{\Delta r} = u_{r,L} - r_L \frac{\Delta u_r}{\Delta r}, \quad (8)$$

with  $\Delta u_r = u_{r,R} - u_{r,L}$  and  $\Delta r = r_R - r_L$ . Multiplying both sides of (8) with the integrating factor  $\exp(-\frac{\Delta u_r}{\Delta r} t)$

gives

$$\frac{d}{dt} \left( r_p e^{-\frac{\Delta u_r}{\Delta r} t} \right) = \left( u_{r,L} - r_L \frac{\Delta u_r}{\Delta r} \right) e^{-\frac{\Delta u_r}{\Delta r} t}. \quad (9)$$

Now integrating both sides of (9) with respect to  $t$  gives the  $r$ -position of the particle as

$$r_p(t) = r_L - u_{r,L} \frac{\Delta r}{\Delta u_r} + C e^{\frac{\Delta u_r}{\Delta r} t}. \quad (10)$$

At  $t = t_0$

$$r_p(t_0) = r_L - u_{r,L} \frac{\Delta r}{\Delta u_r} + C e^{\frac{\Delta u_r}{\Delta r} t_0}, \quad (11)$$

and thus

$$\delta r = r_p(t) - r_p(t_0) = C \left( e^{\frac{\Delta u_r}{\Delta r} t} - e^{\frac{\Delta u_r}{\Delta r} t_0} \right). \quad (12)$$

From Eq. (11), with  $r_p(t_0) = r_0$ , and Eq. (8) at  $t = t_0$  the constant  $C$  follows to

$$C = u_{r,0} \frac{\Delta r}{\Delta u_r} e^{-\frac{\Delta u_r}{\Delta r} t_0}. \quad (13)$$

and thus the radial increment for  $\delta t = t - t_0$  is

$$\delta r = u_{r,0} \frac{\Delta r}{\Delta u_r} \left( e^{\frac{\Delta u_r}{\Delta r} \delta t} - 1 \right) \quad (14)$$

Expanding the exponential term, this scheme is first order in time for the leading contribution. Similarly, for the azimuthal and axial directions, the distances are given by

$$\delta \phi = \frac{u_{\phi,0}}{r_0} \frac{\Delta \phi}{\Delta u_\phi} \left( e^{\frac{\Delta u_\phi}{\Delta r} \delta t} - 1 \right), \quad (15)$$

$$\delta z = u_{z,0} \frac{\Delta z}{\Delta u_z} \left( e^{\frac{\Delta u_z}{\Delta z} \delta t} - 1 \right). \quad (16)$$

The equations of the particle trajectories in the Lagrangian frame are

$$r_p(t) = r_p(t_0) + \delta r, \quad (17)$$

$$\phi_p(t) = \phi_p(t_0) + \delta \phi, \quad (18)$$

$$z_p(t) = z_p(t_0) + \delta z. \quad (19)$$

The temperature field  $T$  is stored at the cell center of the staggered grid as shown in Fig. 1. At first, we interpolate  $T$  at the vertices of the Eulerian grid and then apply trilinear interpolation to calculate the Lagrangian temperature at a known particle position.

### III. TRACER DYNAMICS IN THE CELL

#### A. Tracer trajectories and large-scale circulation

For the Lagrangian simulations, we have selected cylindrical cells which are given in Tab. I keeping the Prandtl number constant ( $Pr = 0.7$ ). We advect  $N_p \sim 10^5$  tracer

Run	$t/t_f$	$Nu_E \pm \sigma$	$Nu_L \pm \sigma$	$N_p$
1	150	$16.73 \pm 0.08$	$16.77 \pm 2.95$	104160
2	150	$16.06 \pm 0.05$	$15.86 \pm 1.37$	81024
3	150	$16.36 \pm 0.03$	$15.70 \pm 0.57$	202860
4	150	$17.44 \pm 0.02$	$16.00 \pm 0.54$	208425
5	150	$17.49 \pm 0.03$	$16.06 \pm 0.54$	272811
6	150	$32.21 \pm 0.32$	$31.75 \pm 4.29$	112320
7	139	$64.31 \pm 0.64$	$65.12 \pm 19.53$	179850

TABLE II: The total integration time  $t/t_f$ , the Eulerian and Lagrangian values of the Nusselt number plus errorbars  $Nu_E$  and  $Nu_L$ , and the total number of tracers  $N_p$  are listed.

particles in the cell (see Tab. II for more details). They are initially seeded in the whole cell and integrated in time for more than 150 time units  $t/t_f$  where  $t_f = H/U_f$  is the free fall time. Here,  $U_f = \sqrt{g\alpha(T_{bottom} - T_{top})H}$ . The statistical analysis is thus conducted over 3000 independent Lagrangian samples, which are separated by  $\Delta t = 0.05t_f$  which corresponds to  $\Delta t = 0.25\tau_\eta$ ,  $0.33\tau_\eta$  and  $0.43\tau_\eta$  for  $Ra = 10^7$ ,  $10^8$  and  $10^9$ , respectively.

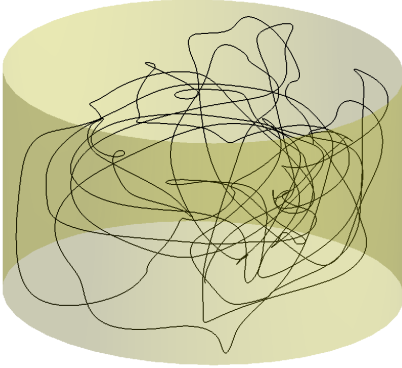


FIG. 3: (Color online) Three-dimensional trajectory of a Lagrangian tracer particle for the simulation at  $Ra = 10^7$  in the cell with aspect ratio  $\Gamma = 1$ . The tracer track is displayed for 100 free-fall time units  $t_f$ .

We visualize the time-evolution of the trajectory of a Lagrangian particle in Fig. 3 for a simulation at  $Ra = 10^7$  in the Rayleigh-Bénard cell with aspect ratio  $\Gamma = 1$ . It seems that this particle travels preferentially along the large-scale circulation (LSC). Fig. 4 plots the time series of the vertical position and various quantities along the same particle path as shown in Fig. 3. The results are qualitatively in agreement with the Eulerian measurements [24] and the Lagrangian measurements [14]. Sharp spikes of the temperature signal appear due to rising and falling plumes close to the hot and cold plates of

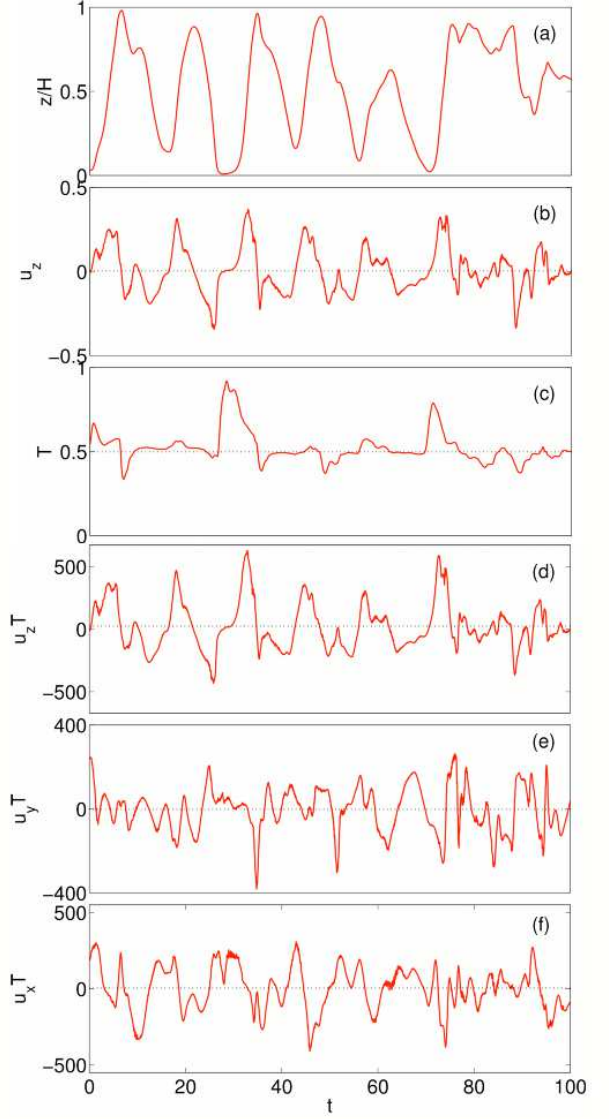


FIG. 4: (Color online) Time series of various quantities along the trajectory of a single Lagrangian tracer particle: (a) the vertical position  $z(t)$  normalized by the cell height  $H$ , (b) the vertical velocity  $u_z(t)$ , (c) the temperature  $T(t)$ , products of velocity components and temperature (d)  $u_z T$ , (e)  $u_y T$  and (f)  $u_x T$ . The dotted lines in some of the panels show the corresponding value of the time average which enters the Lagrangian definition of the Nusselt number as given in Eq. (21). Data are taken along the tracer track which is shown in Fig. 3

the cell. They are correlated with the maxima and minima in the vertical position. The vertical velocity  $u_z(t)$  has zero mean. The convective heat fluxes are shown in Fig. 4(d)-(f). The signals are highly irregular with sharp intermittent peaks. The factor  $\sqrt{RaPr}$  is multiplied to all flux terms  $u_x T$ ,  $u_y T$  and  $u_z T$  in order to get the values of the dimensionless local convective heat flux. Similar to Gasteuil *et al.* [14] we observe strong fluctuations about

the mean value which are 4.8,  $-1.7$  and  $23.4$  for  $u_x T$ ,  $u_y T$  and  $u_z T$ , respectively. It demonstrates that the vertical flux  $u_z T$  is dominantly responsible for the net heat transfer in the cell.

The time series of the vertical tracer position  $z(t)$  shows a rather regular oscillatory form which is caused by the mean wind in the cell. One can therefore extract a typical loop time from all the time series. Motivated by the analysis of Sreenivasan *et al.* [25] for mean wind reversals, we have therefore performed a statistics of the zero-crossings for  $z_i(t)$  with  $i = 1..N_p$ . The mean time interval between two subsequent zero crossings for each tracer track has been determined, and a subsequent Lagrangian ensemble mean,  $\langle \cdot \rangle_L$  has been taken. The latter, which we denote as  $\langle T_{zc} \rangle_L$ , gives a characteristic loop time of the tracers,  $T_l = 2\langle T_{zc} \rangle_L$ . For a fixed Rayleigh number  $Ra = 10^7$ ,  $T_l = 19.4t_f, 17.8t_f$  and  $19.0t_f$  for  $\Gamma = 1, 3$  and  $8$ , respectively.

Translating into a convective time unit  $t_c = H/\langle u^2 \rangle_{V,t}^{1/2}$  (see Ref. [17] for a discussion) gives  $T_l \approx 3.7t_c, 3.4t_c$  and  $3.6t_c$  for  $\Gamma = 1, 3$  and  $8$ , respectively. For a fixed aspect ratio  $\Gamma = 1$ , we find  $T_l = 19.6t_f$  at  $Ra = 10^8$  and  $T_l = 20.6t_f$  at  $Ra = 10^9$ . We see that the characteristic loop time of the tracer is slightly varying but no clear trend when  $\Gamma$  is varied and  $Ra$  is fixed. It seems, therefore, to be independent of the presence of a single-roll or multi-roll LSC. In case of the fixed aspect ratio, a slight increase of  $T_l$  with increasing  $Ra$  is detected. We recall that the velocity fluctuations amplitude decreases with increasing  $Ra$  as reported for example by Verzicco and Camussi [20]. Our observation of a slightly longer loop time seems to be consistent with a reduced amplitude of velocity fluctuations with increasing  $Ra$ . On the basis of the present data, it is however difficult to draw a firm conclusion about the robustness of this trend.

### B. Heat transfer in the Lagrangian frame

Similar to the Eulerian case, where the Nusselt number is given by

$$Nu_E = 1 + \frac{H}{\kappa \Delta T} \langle u_z T \rangle_{V,t}, \quad (20)$$

with  $\langle \cdot \rangle_{V,t}$  being a volume and time average, the Nusselt number in the Lagrangian frame,  $Nu_L$ , is given by [16]

$$Nu_L = 1 + \frac{H}{\kappa \Delta T} \langle u_z T \rangle_{L,t} = \langle Nu_L(t) \rangle_t, \quad (21)$$

where the symbol  $\langle \cdot \rangle_{L,t}$  denotes an averaging over all trajectories and time. We compute the time series of the heat transfer in the Lagrangian frame and compare with its value in the Eulerian frame in Fig. 5 for a simulation at  $Ra = 10^7$  in the cell with aspect ratio  $\Gamma = 1$ . The time averaging of  $Nu_L(t) = 1 + H/(\kappa \Delta T) \langle u_z(t) T(t) \rangle_L$  curve from  $t = 40$  to  $200$  yields  $Nu_L = 16.77$ , which almost exactly matches the corresponding value of the

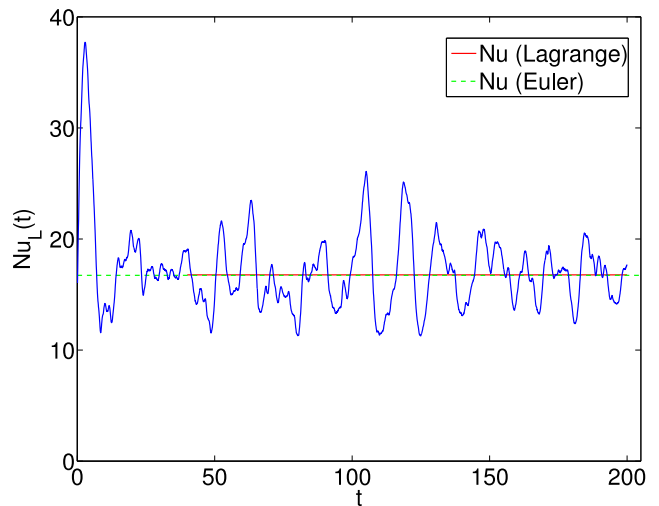


FIG. 5: (Color online) Graph of  $Nu_L(t)$  which is averaged over  $\sim 10^5$  tracer paths. The temporal mean value of  $Nu_L = \langle Nu_L(t) \rangle_t$  (see Eq. (21)) between time  $t = 40 - 200$  is  $Nu_L = 16.77$ , which almost exactly matches with the corresponding Eulerian value  $Nu_E = 16.73$  as listed in Table II.

Eulerian simulation, which was  $Nu_E = 16.73$  as provided in Tab. II. Similar result is achieved for the simulation conducted at  $Ra = 10^8$  in the same cell, for which  $Nu = 32.21$  and  $Nu_L = 31.75$  with a deviation of 1.5% from  $Nu_E$ . The results also validate our interpolation schemes and the time step sizes for the Lagrangian simulations, which are accurate enough to reproduce flow quantities of the corresponding Eulerian simulations in turbulent convection. In contrast, recent experiments by [14] obtained a value of  $Nu_L$  almost twice as large as the Eulerian case. This discrepancy is due to the fact that their [14] mobile sensor traversed preferentially along the mean flow circulation path and hence the contribution from the rest of the volume was missing in their Nusselt number measurement.

At the beginning of the  $Nu_L(t)$  curve in Fig. 5, there is a large overshoot from mean, which generally appears when the majority of the particles follow the LSC path or the particles are not seeded uniformly in the flow. We also observe strong oscillations in  $Nu_L(t)$  for all the simulations listed in Tab. II. Strong fluctuations around the mean result in large standard deviation  $\sigma$ . The value of  $\sigma$  decreases with increasing  $\Gamma$ . When the number of particles was increased (case:  $N_p \approx 2.5 \times 10^5$ ,  $Ra = 10^7$  and  $\Gamma = 1$ ; the results are not shown here), the convergence of  $Nu_L(t)$  was achieved within a shorter period of time. It can be concluded that the number of tracer particles should be sufficiently large and they should be uniformly seeded in the domain for faster statistical convergence of  $Nu_L(t)$ .

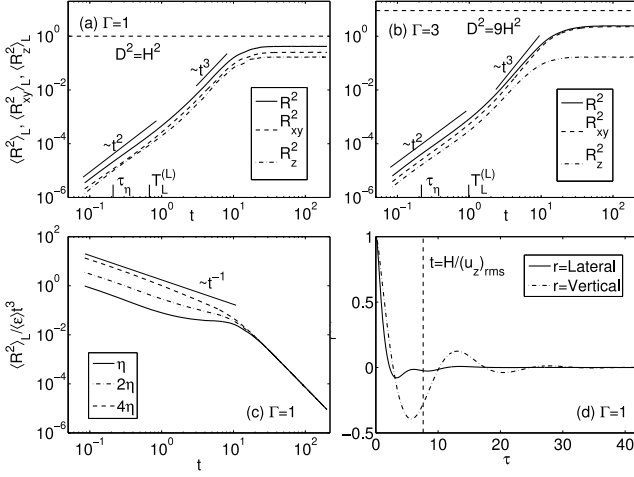


FIG. 6: Pair dispersion as in Eqs. (22)–(24): (a) aspect ratio  $\Gamma = 1$ , (b)  $\Gamma = 3$ , (c) pair dispersion normalized by  $\langle \epsilon \rangle t^3$  for three initial separations,  $\eta$ ,  $2\eta$  and  $4\eta$ , with  $\eta$  the Kolmogorov length and (d) the autocorrelation functions of the lateral and vertical velocities for  $\Gamma = 1$  as given in Eqs. (25) and (26), respectively. The Kolmogorov time  $\tau_\eta$  (see Eq. (29)) and the lateral Lagrangian time  $T_L^{(L)}$  (see Eq. (28)) are marked on the time axis in (a) and (b). The horizontal dashed lines in (a) and (b) denote  $D^2 = \Gamma^2 H^2$ . The vertical dashed line in (d) represents the characteristic time required by a particle to travel the cell of height  $H$ . The analysis is conducted at  $Ra = 10^7$  with  $4.16 \times 10^8$  and  $3.24 \times 10^8$  statistical samples for  $\Gamma = 1$  and  $\Gamma = 3$ , respectively.

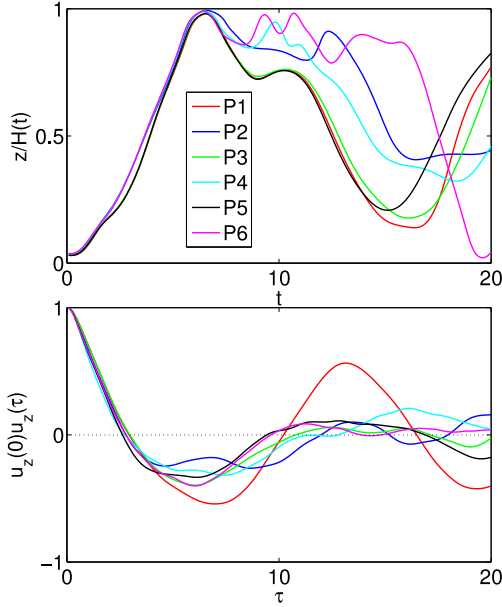


FIG. 7: (Color online) Relation between the vertical coordinate and the anti-correlation of vertical velocity. In the top panel, we show the  $z(t)$ -component of 6 particle trajectories, which were seeded close to the bottom plate. The corresponding product  $u_z(0)u_z(\tau)$  along each trajectory which enters into the definition of the Lagrangian integral time is shown in the bottom panel.

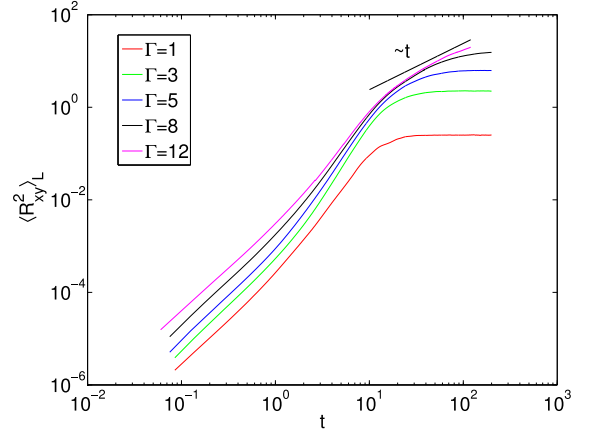


FIG. 8: (Color online) Time evolution of the lateral pair dispersion as a function of the aspect ratio  $\Gamma$ . Data are for  $Ra = 10^7$ . The lowermost curve is for  $\Gamma = 1$  and the uppermost for  $\Gamma = 12$ .

#### IV. LAGRANGIAN PAIR DISPERSION

The pair dispersion measures the relative separation of a pair of tracer particles traversing along their trajectories and is defined as

$$R^2(t) = \langle [\mathbf{x}_p(t) - \mathbf{x}_p(t_0)]^2 \rangle_L. \quad (22)$$

Since convective turbulence is inhomogeneous, we decompose the distance vector into two parts – the lateral part  $\mathbf{R}_{xy}(t)$  and the vertical part  $\mathbf{R}_z(t)$ . Their contributions to the total dispersion  $R^2(t)$  are given by

$$R_{xy}^2(t) = \langle [x_p(t) - x_p(t_0)]^2 + [y_p(t) - y_p(t_0)]^2 \rangle_L \quad (23)$$

$$R_z^2(t) = \langle [z_p(t) - z_p(t_0)]^2 \rangle_L. \quad (24)$$

This decomposition is chosen in order to relate our results to the findings in [15, 16]. We also compute the autocorrelation functions of the velocity components as

$$C_{xy}(\tau) = \frac{\langle \mathbf{u}_{xy}(t+\tau) \cdot \mathbf{u}_{xy}(t) \rangle_{L,t}}{\langle |\mathbf{u}_{xy}|^2 \rangle_{L,t}}, \quad (25)$$

$$C_z(\tau) = \frac{\langle u_z(t+\tau)u_z(t) \rangle_{L,t}}{\langle u_z^2 \rangle_{L,t}}. \quad (26)$$

Here  $C_{xy}(\tau)$  is the autocorrelation coefficient for the lateral tracer velocities  $\mathbf{u}_{xy} = u_x \mathbf{e}_x + u_y \mathbf{e}_y$ , with  $\mathbf{e}_x$  and  $\mathbf{e}_y$  are the unit vectors in  $x$  and  $y$  directions, respectively,  $C_z(\tau)$  is for the vertical velocity  $u_z$ , and  $\tau$  is the time lag. The vertical and lateral Lagrangian times,  $T_L^z$  and  $T_L^{xy}$  are obtained by integrating  $C_z(\tau)$  and  $C_{xy}(\tau)$  as

$$T_L^z = \int_0^\infty C_z(\tau) d\tau \quad (27)$$

$$T_L^{xy} = \int_0^\infty C_{xy}(\tau) d\tau, \quad (28)$$



$\Gamma$	1	3	5	8
$\tau_\eta$	0.211	0.215	0.213	0.206
$T_L^{xy}$	0.68	0.98	1.21	1.16

TABLE III: Kolmogorov time scale and lateral Lagrangian integral times. Data are for  $Ra = 10^7$  and different aspect ratios.

and the Kolmogorov time  $\tau_\eta$  is given by

$$\tau_\eta = \sqrt{\frac{\nu}{\langle \epsilon \rangle}}. \quad (29)$$

Figures 6(a) and (b) plot the total dispersion,  $R^2$ , as well as the lateral,  $R_{xy}^2$ , and vertical,  $R_z^2$ , contributions. Two aspect ratios are selected, namely  $\Gamma = 1$  and 3 for simulations at  $Ra = 10^7$ . Initially, the quantities grow with  $R^2 \sim t^2$ , which corresponds to the ballistic dispersion. After the ballistic growth, a transition to a regime with a growth law of  $R^2 \sim t^3$  occurs. Similar observations were made for fluid turbulence [26] and for convective turbulence in an extended layer [15, 16]. The range is however too short to conclude if this is a Richardson-like regime [8] or not. The horizontal dashed lines mark the square of the cell diameter, the limit which cannot be exceeded by pair separation. The finite size of the cell suppresses also an eventual Taylor diffusion regime with  $R^2 \sim t$  and as a result the dispersion levels off, which is different from the Cartesian cells with periodic side-walls [15, 16]. The Kolmogorov time  $\tau_\eta$  and the lateral Lagrangian integral time  $T_L^{xy}$  as a function of the aspect ratio are listed in Tab. III. While the Kolmogorov time remains nearly unchanged with an increase of  $\Gamma$ , the lateral Lagrangian integral time increases by almost 100% for an increase of  $\Gamma$  from 1 to 5. This would be in line with a stronger correlation of the lateral velocity components which could arise in the multi-roll LSC case.

Recent numerical Lagrangian studies in homogeneous isotropic turbulence by Sawford *et al.* [29] yielded a sensitive dependence of the pair dispersion on the initial pair separation. This was confirmed in the case of convective turbulence in an extended layer [16]. In addition it was found there that the intermediate evolution of the dispersion in thermal convection depends on the seeding height of the tracer pairs since convective turbulence is inhomogeneous in the vertical direction. Here, we repeat these studies. In Fig. 6(c), the pair dispersion normalized by  $\langle \epsilon \rangle t^3$  is plotted for three different initial separations, namely  $\eta$ ,  $2\eta$  and  $4\eta$ , with  $\eta = \nu^{3/4}/\langle \epsilon \rangle^{1/4}$  the Kolmogorov length. The figure shows that a plateau, i.e.  $R^2 \sim t^3$ , is reached for the smallest initial separation only.

The autocorrelation functions of the lateral and vertical velocities are shown in Fig. 6(d) for one run. The results are in agreement with [15]. The vertical velocity is strongly anticorrelated to the lateral one. This strong anticorrelation is in line with the rapid upward

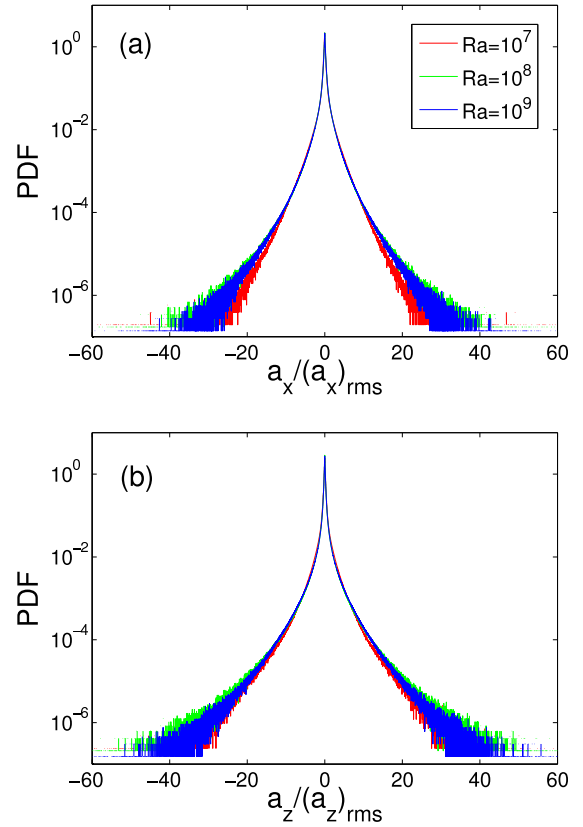


FIG. 9: (Color online) The probability density functions of the acceleration components for different Rayleigh numbers at  $\Gamma = 1$ . Amplitudes are normalized by the corresponding root-mean-square value. (a) Component  $a_x$ . (b) Component  $a_z$ .

and downward motions as indicated by the signals of velocity components along a tracer path in Fig. 4, in which fluctuations in  $u_z(t)$  are stronger than those in  $u_x(t)$  and  $u_y(t)$  (time signals of  $u_x$  and  $u_y$  are not shown here). In order to demonstrate this more quantitatively, we plot in Fig. 7 the vertical displacement of the Lagrangian particles and the corresponding integrand of definition  $T_L^{(z)}$  (see Eq. 28) for 6 tracers that are initially seeded close to bottom boundary layer. The pronounced minimum of  $u_z(0)u_z(\tau)$  coincides with the reversal point of  $z(t)$  close to the top boundary layer.

Fig. 8 shows the dependence of the long-time behavior of the lateral dispersion on the aspect ratio. Only for the largest aspect ratio ( $\Gamma = 12$ ) a diffusion limit with  $R_{xy}^2(t) \sim t$  is obtained. It underlines an important difference in contrast to configurations with periodic boundary conditions in the lateral directions. In our case, the dispersion is additionally constrained by the sidewalls for small-aspect-ratio systems.

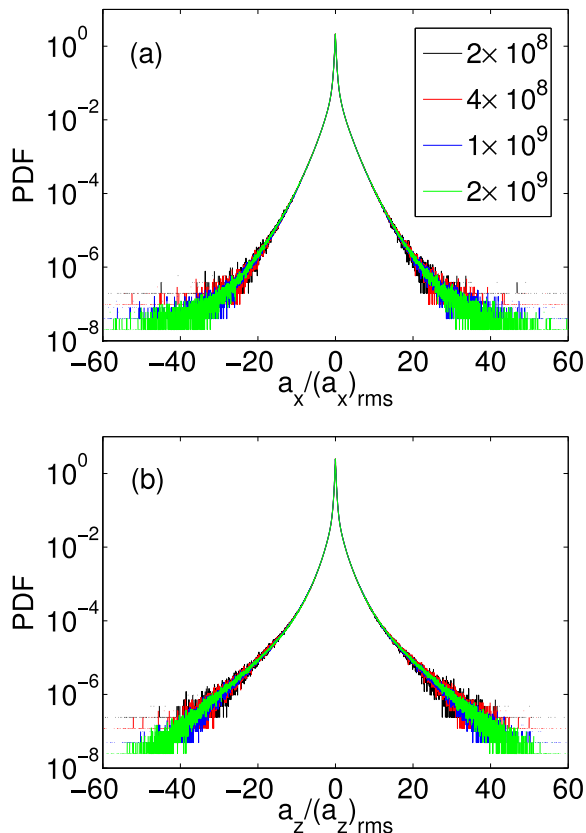


FIG. 10: (Color online) The convergence of the probability density functions of one lateral and the vertical acceleration components for different  $Ra = 10^7$  and  $\Gamma = 1$ . Data are for  $2 \times 10^8$ ,  $4 \times 10^8$ ,  $10^9$ , and  $2 \times 10^9$  sample events.

## V. ACCELERATION STATISTICS

Finally, we report the probability density function (PDF) of acceleration components along three-dimensional trajectories. In Fig. 9 we compare data for three different Rayleigh numbers with fixed aspect ratio  $\Gamma = 1$ . Both lateral and vertical acceleration components show no systematic trend with  $Ra$ . The stretched exponential form is similar to those reported in laboratory experiments [3–5] and DNS simulations of turbulent convection [15, 16].

A critical issue of numerical and experimental Lagrangian studies – not only in turbulent convection – is the statistical convergence, which requires to determine, for example, a fourth-order moment, such as the flatness  $F(a_k)$ . In Lagrangian turbulence, the situation becomes particularly problematic since the tails of the PDFs are found to be strongly scattered [30, 31]. The statistical uncertainty is also manifested in the scattered tails of the PDFs in Fig. 9 although more than  $2 \times 10^8$  data points have been included. In Fig. 10, we ran the simulation for significantly longer period such that the number of samples became one order of magnitude larger. The tails

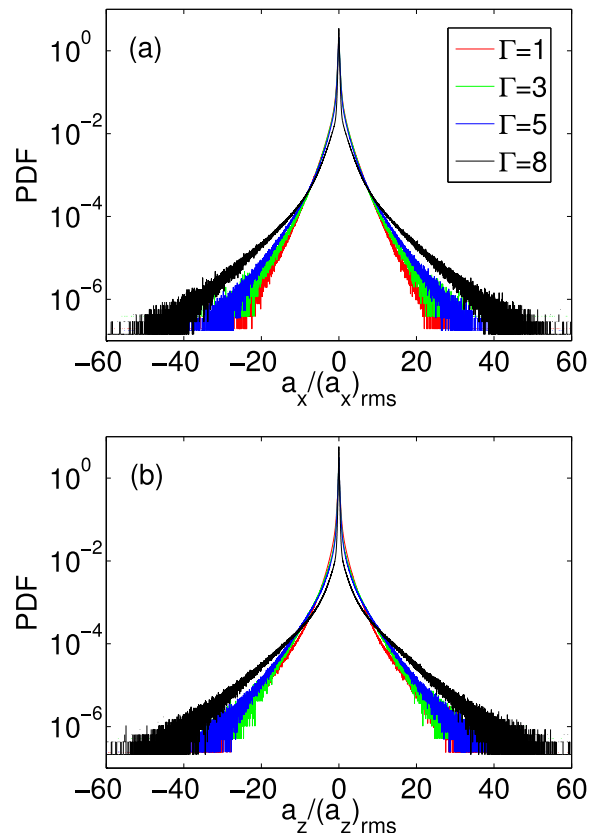


FIG. 11: (Color online) The probability density functions of the acceleration components. (a) Component  $a_x$ . (b) Component  $a_z$ . The uppermost graph is for the largest aspect ratio in both panels.

become less scattered and more extended with increasing number of samples. The data indicate that the convergence in the vertical direction is slower than in the lateral direction. Nevertheless, the scatter for the fourth order moments remains so strong that the flatness is obtained with a big error bar only. The flatness is defined as

$$F(a_k) = \frac{\langle a_k^4 \rangle_{L,t}}{\langle a_k^2 \rangle_{L,t}^2} \quad (30)$$

with  $k = x, y$  and  $z$ . We found that  $F(a_z) = 89 \pm 18$  for  $4 \times 10^9$  samples.

The dependence on the aspect ratio  $\Gamma$  is demonstrated in Fig. 11. It can be seen that the tails of the PDF of  $a_x$  grow with increasing aspect ratio, which implies that less constrained lateral motion causes larger acceleration magnitudes. Meandering of the tracers among different LSC rolls [17] will probably contribute to larger amplitudes in the acceleration as well. Interestingly, a similar but weaker trend holds for the vertical acceleration component as well.



## VI. SUMMARY AND DISCUSSION

We have presented DNS studies on the Lagrangian tracer particle dynamics in turbulent Rayleigh-Bénard convection. The main objective of this work was to investigate how the finiteness of the cell size in convection impacts the motion, dispersion and acceleration of the tracer particles. We developed an interpolation scheme for the staggered computational mesh, which was used in the Eulerian simulation. Our interpolation scheme reproduces accurately the global heat transfer in the Lagrangian frame  $Nu_L$ , which matches the corresponding value in the Eulerian frame  $Nu_E$ . We detected however large fluctuations of  $Nu_L(t)$  about the mean value since the majority of the tracers is moving along the mean circulation path in the cell. Our studies suggest that either a large number of particles or a very long time integration period are necessary for faster convergence of  $Nu_L(t)$ . The convergence is found to be slower for a non-uniform initial tracer seeding.

In the pair dispersion analysis, we confirmed the initial ballistic regime ( $R^2 \sim t^2$ ) and a very short-range regime with  $R^2 \sim t^3$  which have also been found in other studies on convection [15, 16] and simulations of homogeneous isotropic turbulence in a periodic cube [26, 29]. The finite size of the convection cell suppresses the dispersion limit; hence a Taylor-like regime ( $R^2 \sim t$ ) is absent for  $\Gamma < 8$  in our studies as opposed to [15]. The autocorrelations of the vertical velocity component are strongly anti-correlated. This is in line with [15] and seems to be associated with the characteristic structures – the thermal plumes – present in convection. These structures have a strong influence on the vertical tracer motion. In

particular they cause the reversals in the tracer tracks, namely when a particle hits the top or bottom plates. While we did not observe a Rayleigh-number-dependence of the acceleration statistics, a systematic dependence of the PDFs of the acceleration components on  $\Gamma$  was obtained. To conclude, the basic Lagrangian properties we studied in the present work agree qualitatively with those in previous studies, e.g. in [15, 16]. The additional variation of the aspect ratio is in line with changes in the large-scale circulation in the convection cell, which affects the Lagrangian tracer dispersion and acceleration.

Our studies complemented the only existing Lagrangian laboratory experiment on convection by Gasteuil *et al.* [14]. We could confirm qualitatively some results obtained in their experiments. Further experimental and numerical studies in the large aspect ratio regime are desirable and necessary. Similar to the Eulerian case, we can expect the aspect ratio dependence to disappear for sufficiently large values of  $\Gamma$ .

## Acknowledgements

We wish to thank Oleg Zikanov for discussions and the Jülich Supercomputing Centre (Germany) for support with computing resources on the JUROPA cluster under grant HIL03. This work is also supported by the Deutsche Forschungsgemeinschaft (DFG) under grant SCHU1410/2-1 and by the Heisenberg Program of the DFG under grant SCHU 1410/5-1. JS acknowledges partial travel support by the European COST Action MP0806 “Particles in turbulence”.

- 
- [1] P. K. Yeung, *Annu. Rev. Fluid Mech.* **34**, 115 (2002).
  - [2] F. Toschi and E. Bodenschatz, *Annu. Rev. Fluid Mech.* **41**, 375 (2009).
  - [3] A. La Porta, G. A. Voth, A. M. Crawford, J. Alexander, and E. Bodenschatz, *Nature* **409**, 1017 (2001).
  - [4] N. Mordant, J. Delour, E. Léveque, A. Arnéodo, and J. F. Pinton, *Phys. Rev. Lett.* **89**, 254502 (2002).
  - [5] G. A. Voth, A. La Porta, A. M. Crawford, J. Alexander, and E. Bodenschatz, *J. Fluid Mech.* **469**, 121 (2002).
  - [6] W. Braun, F. De Lillo, and B. Eckhardt, *J. Turbul.* **7**, N62 (2006).
  - [7] G. K. Batchelor, *Quart. J. R. Meteorol. Soc.* **76**, 133 (2009).
  - [8] L. F. Richardson, *Proc. R. Soc. London, Ser. A* **110**, 709 (1926).
  - [9] G. Ahlers, S. Grossmann, and D. Lohse, *Rev. Mod. Phys.* **81**, 503 (2009).
  - [10] R. du Puits, C. Resagk, and A. Thess, *Phys. Rev. E* **75**, 016302 (2007).
  - [11] D. Lohse and K.-Q. Xia, *Annu. Rev. Fluid Mech.* **42**, 335 (2010).
  - [12] B. Castaing, G. Gunaratne, F. Heslot, L. P. Kadanoff, A. Libchaber, S. Thomae, X.-Z. Wu, S. Zaleski, and G. Zanetti, *J. Fluid Mech.* **204**, 1 (1989).
  - [13] M. S. Emran and J. Schumacher, *J. Fluid Mech.* **611**, 13 (2008).
  - [14] Y. Gasteuil, W. L. Shew, M. Gibert, F. Chillá, B. Castaing, and J. F. Pinton, *Phys. Rev. Lett.* **99**, 234302 (2007).
  - [15] J. Schumacher, *Phys. Rev. Lett.* **100**, 134502 (2008).
  - [16] J. Schumacher, *Phys. Rev. E* **79**, 056301 (2009).
  - [17] J. Bailon-Cuba, M. S. Emran, and J. Schumacher, *J. Fluid Mech.*, in press (2010).
  - [18] R. J. A. M. Stevens, R. Verzicco, and D. Lohse, *J. Fluid Mech.* **643**, 495 (2010).
  - [19] R. Verzicco and P. Orlandi, *J. Comp. Phys.* **123**, 402 (1996).
  - [20] R. Verzicco and R. Camussi, *J. Fluid Mech.* **477**, 19 (2003).
  - [21] G. Grötzbach, *J. Comput. Phys.* **49**, 241 (1983).
  - [22] P. N. Schwarztrauber, *SIAM J. Num. Anal.* **11**, 1136 (1974).
  - [23] W. Schönfeld, *J. Marine Systems* **6**, 529 (1995).
  - [24] X.-D. Shang, X.-L. Qiu, P. Tong, and K.-Q. Xia, *Phys. Rev. E* **70**, 026308 (2004).
  - [25] K. R. Sreenivasan, A. Bershadskii, and J. J. Niemela,

- Phys. Rev. E **65**, 056306 (2002).
- [26] G. Boffetta and I. M. Sokolov, Phys. Rev. Lett. **88**, 094501 (2002).
- [27] L. Chevillard, B. Castaing, E. L  v  que, and A. Arneodo, Physica D **218**, 77 (2006).
- [28] S. B. Pope, *Turbulent flows*. Cambridge University Press, 2000.
- [29] B. L. Sawford, P. K. Yeung, and J. F. Hackl, Phys. Fluids **20**, 065111 (2008).
- [30] K. R. Sreenivasan and J. Schumacher, Phil. Trans. Roy. Soc. A **368**, 1561 (2010).
- [31] N. Mordant, A. M. Crawford, and E. Bodenschatz, Physica D **193**, 245 (2004).